Volume and concentration dosing in picolitres using a two-channel microfluidic AFM cantilever

Verlinden, E. J.; Madadelahi, M.; Sarajlic, E.; Shamloo, A.; Engel, A. H.; Staufer, U.; Ghatkesar, M. K.

Important note
To cite this publication, please use the final published version (if applicable).
Please check the document version above.

PAPER

Check for updates

Volume and concentration dosing in picolitres using a two-channel microfluidic AFM cantilever†

E. J. Verlinden,‡[a] M. Madadelahi,‡[a,b,c] E. Sarajlic,[d] A. Shamloo,[b] A. H. Engel,[e] U. Staufer[a] and M. K. Ghatkesar [ID] *[a]

We introduce a two-channel microfluidic atomic force microscopy (AFM) cantilever that combines the nanomechanical sensing functionality of an AFM cantilever with the ability to manipulate fluids of picolitres or smaller volumes through nanoscale apertures near the cantilever tip. Each channel is connected to a separate fluid reservoir, which can be independently controlled by pressure. Various systematic experiments with fluorescent liquids were done by either injecting the liquids from the on-chip reservoir or aspirating directly through the nanoscale apertures at the tip. A flow rate analysis of volume dosing, aspiration and concentration dosing inside the liquid medium was performed. To understand the fluid behaviour, an analytical model based on the hydrodynamic resistance, as well as numerical flow simulations of single and multi-phase conditions were performed and compared. By applying pressures between −500 mbar and 500 mbar to the reservoirs of the probe with respect to the ambient pressure, flow rates ranging from 10 fl s^{-1} to 83 pl s^{-1} were obtained inside the channels of the cantilever as predicted by the analytical model. The smallest dosing flow rate through the apertures was 720 fl s^{-1}, which was obtained with a 10 mbar pressure on one reservoir and ambient pressure on the other. The solute concentration in the outflow could be tuned to values between 0% and 100% by pure convection and to values between 17.5% and 90% in combination with diffusion. The results prove that this new probe enables handling multiple fluids with the scope to inject different concentrations of analytes inside a single living cell and also perform regular AFM functionalities.

1. Introduction

The capability to dose multiple reagents at a given location will enable performing controlled (bio)chemical reactions. If this can be done in small volumes (≤pl, 1000 μm^3 = 1 pl), it will give unprecedented access to perform reactions close to or even inside single cells. In addition, if the concentration of the reagents can also be controlled *in situ* in such small volumes, it will increase the throughput of chemical processes under investigation in terms of dynamic titration of the reagents. Furthermore, it also increases the efficiency of the amount of chemicals used.

Non-contact dosing of picolitre volumes on a surface in an air environment can be achieved by the inkjet printing method.[1–3] However, aspiration and dosing inside another liquid is not possible with this method. For dosing and aspirating such small volumes inside another liquid in "open space" (outside the fluidic channels), microfluidic glass capillaries with controlled channel pressure are typically used.[4]

Instead of a single aperture, two apertures next to each other were also introduced.[5] By controlled injection of the analyte through one aperture and aspiration of both the analyte and the surrounding medium through another, a hydrodynamic confinement flow of the analyte was achieved (by using higher flow convection rates compared to analyte diffusion). It enabled delivering analytes confined to a 100 μm diameter in "open space" to perform a variety of local studies on 2D cell cultures and tissue sample surfaces on a centimeter scale.[6–8] Based on this hydrodynamic confinement flow, several fluid probe varieties made from silicon, polydimethysiloxane (PDMS) and SU8 were reported.[9–13] Without hydrodynamic confinement, dosing over a surface area of 100 μm diameter and nanolitre volumes was possible. The functionality of such probes was confined only for local fluid manipulation (dosing and aspiration).

[a]*Department of Precision and Microsystems Engineering, Delft University of Technology, The Netherlands. E-mail: m.k.ghatkesar@tudelft.nl; Fax: +31 (0) 15-2782299; Tel: +31 (0) 15-27 82299*
[b]*Department of Mechanical Engineering, Sharif University of Technology, Iran*
[c]*School of Engineering and Sciences, Tecnologico de Monterrey, Monterrey, Mexico*
[d]*SmartTip B.V., Enschede, The Netherlands*
[e]*Department of Bionanoscience, Delft University of Technology, The Netherlands*
†Electronic supplementary information (ESI) available. See DOI: 10.1039/C9NR10494A
‡These authors contributed equally to this work.

By using scanning ion conductance microscopy (SICM), apart from imaging the topography of surfaces, dosing and aspiration of liquids were also performed. Glass tubes of diameters ranging from 90 nm–130 nm were used to directly deliver analytes. By controlling the voltage between the liquid inside the glass tube and the surrounding fluid, dosing of analytes into the "open space" was achieved.[14–17] The functionality was extended by using double-barrel tubes[18] and co-axial dual glass pipettes.[19]

If local small volume fluid manipulation can be done using an atomic force microscopy cantilever, then high-resolution topography imaging and force-spectroscopy will become possible simultaneously, thus increasing the versatility of the fluidic probe. With this idea, a microfluidic atomic force microscopy (AFM) cantilever was fabricated in silicon nitride and fluid-force microscopy (FluidFM) was introduced.[20–23] A force-controlled injection (dosing) and extraction of sub-cellular contents from a single cell became possible.[24–27] The force-controlled dosing platform was extended to contain 4 fluidic reservoirs.[28] However, each reservoir was connected to an individual probe; therefore, simultaneous dosing of multiple liquids at the desired location was not possible.

In this work, we present a two-channel microfluidic AFM cantilever with two apertures near the tip apex. Each channel is connected to a different reservoir, but dosing/aspiration is performed from a single tip located at the free end of the cantilever. By controlling the pressure on the reservoirs, femtolitre to picolitre volume of liquids can be controlled in "open space", at different combinations of reservoir liquids. A delicate balance between the diffusion of analytes and fluid flow convection enables precise dosing of fluid volume and analyte concentration.

A schematic of the microfluidic AFM cantilever with two on-chip reservoirs is shown in Fig. 1. The reservoirs are connected to a suspended microfluidic cantilever with two separate channels, Leg 1 and Leg 2. The channels on the cantilever merge inside the pyramidal tip, from where the fluid can exit through two apertures located near the tip apex. The figure also shows that the cantilever is immersed in water (blue colour) and one of the reservoirs is filled with fluorescein

(green) and the other is empty. Three different situations of dosing, aspirating and co-dosing that were investigated in this work are also shown.

2. Two channel microfluidic AFM cantilever probe

The microfluidic AFM cantilever probe consists of two separate microfluidic channels connected at the probe tip on the one end and separate on-chip fluidic reservoirs at the other end. The channels individually consist of an on-chip channel (non-suspended) and a cantilever channel (suspended) represented by Leg 1 and Leg 2, Fig. 2A and B. The channels further split into two separate channels at the tip, Fig. 2C. All four channels at the tip are merged into a single pyramid, Fig. 2C, a pyramidal tip zoom-in. The pyramidal probe tip combines liquids from both channels before dosing through two nanoscale apertures on the tip wall, Fig. 2D and E. The tip sharpness was maintained by strategically placing the apertures. The probes were made from silicon-rich silicon nitride by a process described elsewhere.[29,30] The microchannels were prepared by the removal of an encapsulated sacrificial polycrystalline silicon layer. To obtain a proper separation of the fluidic channels in the pyramidal tip and to merge these channels together at the tip apex, a rather complex processing based on corner lithography was used. Because of this complexity, a small
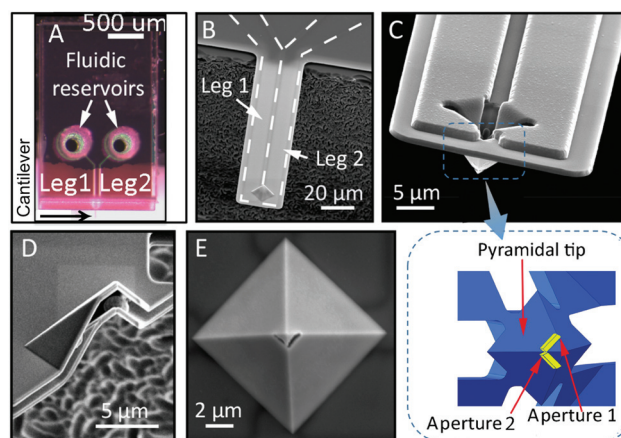
Fig. 2 (A) Optical microscopy image of a two-channel microfluidic AFM cantilever chip, reservoir-side of the chip. The fluidic reservoirs connect to the two legs of the cantilever, suspended at the front. (B) The SEM picture of the cantilever viewed from the tip-side, with the pyramidal tip pointing upwards. The side-walls of the two channels are indicated by white dashed lines. (C) An isometric view of the cantilever free end, with the pyramidal tip pointing downwards. The channel widths decrease drastically as they merge into a chamber within the pyramidal tip. A zoom-in of the pyramid internal structure shown as a CAD drawing in the dashed box. All channels merge in a small internal pyramid. The pyramid had two apertures (marked yellow) on the side-wall. (D) A cross-section of the pyramid tip pointing upwards was obtained by focused ion beam milling. (E) A close view of the cantilever tip external pyramid pointing upwards, with two side-apertures on the pyramid wall. The sharp tip apex was intact.
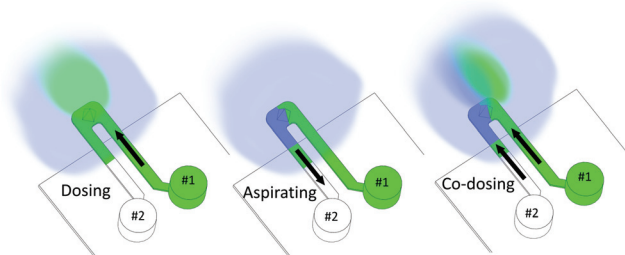

Fig. 1 Schematic of the microfluidic AFM cantilever chip. There are two on-chip reservoirs, two on-chip channels and a suspended cantilever with two channels. Three different cases of dosing liquid from reservoir 1 (fluorescein) into water (blue), aspirating water into channel 2 and co-dosing of water from channel 2 and liquid from channel 1 that are investigated are also shown.

Table 1 Two-channel microfluidic AFM cantilever dimensions

Parameter	Dimension
Total length	130 µm
Total width	28 µm
Channel length	121 µm
Channel width	9.5 µm
Channel height	1 µm
Wall thickness	200 nm
Aperture sizes	0.3 µm × 1 µm
	0.37 µm × 1 µm

difference between the size of the apertures on different sidewalls of the pyramidal tip can occur. The intention was to create a single aperture of 0.3 µm × 2 µm, with 0.3 µm × 1 µm on each face of the pyramid merging at the corner. However, the corner remained underetched (due to corners being slightly thicker than the faces) resulting in two apertures. The under-etched corner should have minimum influence on the fluidic resistance. The fundamental resonance frequency was found to be typically around 190 kHz and a stiffness of 3.9 N m^{-1} was obtained (in air, using the Sader method). The dimensions of our two-channel microfluidic AFM cantilever are summarized in Table 1. An AFM image taken by the probe in the tapping mode is given in ESI: section 1 and Fig. S1.†

3. Device modeling

3.1 Numerical model

A numerical model was developed to understand the flow velocity and concentration profiles inside the microfluidic AFM cantilever for various applied pressure conditions. Both single-phase (only liquid) and two-phase (liquid and gas) fluids were simulated. See ESI section 2 and Fig. S2.†

3.1.1 Single-phase fluids. The Navier–Stokes (eqn (1)) and the convection–diffusion (eqn (2)) equations were solved simultaneously to describe the fluid behaviour.[31]

$$\rho\left(\frac{\partial \vec{v}}{\partial t} + (\vec{v} \cdot \nabla)\vec{v}\right) = -\overrightarrow{\nabla P} + \mu \nabla^2 \vec{v}, \tag{1}$$

$$\frac{\partial C}{\partial t} + \vec{v} \cdot \nabla C = D_m \nabla^2 C, \tag{2}$$

where $\vec{v}$ is the velocity vector (m s^{-1}), P is the pressure (Pa), t is the time (s), μ is the dynamic viscosity (Pa s), ρ is the density (k m^{-3}), C is the concentration (mol m^{-3}) and D_m is the molecular diffusion coefficient (m^2 s^{-1}). Based on the experimental values from the literature,[32] the modelled fluid, fluorescein in water, was assumed to have a viscosity of 0.001 Pa s, a density of 1000 kg m^{-3} and a diffusion coefficient of 6.4×10^{-10} m^2 s^{-1}. To limit the computation time, only the channels on the cantilever (Leg 1 and Leg 2 cantilever channels) were simulated. The geometry of the cantilever was generated based on the dimensions measured from SEM micrographs (see Fig. 2) and lithography masks. To compensate for the pressure loss over the non-modelled part of the

microfluidic channels (the on-chip channel), applied pressures imposed on the model boundaries were decreased accordingly.

Two approaches were investigated for numerical simulations. In the first approach, the flow and the concentration profile in the cantilever was simulated considering that the pressure outside the aperture is at ambient pressure and no fluid was present. For dosing, it was considered that the cantilever was initially filled with water and the following three boundary conditions were used. (1) The pressures applied on Leg 1 and Leg 2 were constant and the pressure outside the aperture was at ambient pressure. (2) A constant concentration ($C = 0.421$ mol m^{-3}) of the liquid was available on Leg 1. (3) For Leg 2 and apertures, a no-flux boundary condition i.e., no concentration gradient occurs at the boundary surface, is considered. It is expressed as $-\vec{n} \cdot (D_m \vec{\nabla} C) = 0$, where $\vec{n}$ is the unit normal vector of the corresponding no-flux boundary surface. For aspiration, it was assumed that the cantilever was initially filled with fluorescein ($C = 0.421$ mol m^{-3}) and the following three boundary conditions were used. (1) The pressures applied on Leg 1 and Leg 2 were constant and the pressure outside the aperture was at ambient pressure. (2) A constant solute concentration ($C = 0.421$ mol m^{-3}) in Leg 1 and ($C = 0$ mol m^{-3}) at apertures was available. (3) For Leg 2, a condition of $-\vec{n} \cdot (D_m \vec{\nabla} C) = 0$, where $\vec{n}$ is the unit normal vector of the corresponding no-flux boundary surface, was considered. See ESI: section 2 and Fig. S3.†

In the second approach, 600 µm^3 of fluid surrounding the probe tip aperture was added to the computational domain. The boundary conditions on the solid walls and the inlet/outlet of the cantilever were similar to the previous approach. However, for the apertures, for the far-field boundaries, an open boundary condition with zero stress was applied for the fluid flow and no-flux was considered for the concentration. All of the mentioned equations and boundary conditions were solved using the Finite Element Method (FEM). See ESI: section 2, Fig. S3 and Movie 1.†

3.1.2 Two-phase fluids. In this Finite Volume Method (FVM) simulation, the conservation of momentum (eqn (3)) and mass (eqn (4)) were solved to capture the meniscus behaviour.[33,34]

$$\rho\left(\frac{\partial \vec{v}}{\partial t} + (\vec{v} \cdot \nabla)\vec{v}\right) = -\overrightarrow{\nabla p} + \nabla \cdot \left(\mu\left(\nabla \vec{v} + (\nabla \vec{v})^T\right)\right) + \vec{F}, \tag{3}$$

$$\frac{\partial \rho \alpha}{\partial t} + \nabla \cdot (\rho \alpha \vec{v}) = 0, \tag{4}$$

where $\vec{F}$ is the volumetric surface tension force in N m^{-3} and α is the volume fraction. Similar to the first approach mentioned in the single-phase section, the cantilever was considered as the computational domain and no external fluids were considered due to the huge computational time. For all solid walls, the no-slip boundary condition was considered and it was assumed that the fluid flow on the inlet was constant. See ESI: section 2, Fig. S4 and Movie 2.†

3.2. Analytical model

3.2.1 Flow rate. An analytical model, based on the electrical circuit analogy, was used in order to qualitatively understand the flow behavior inside the fluidic channel. As the flow is pressure-driven and laminar, a simplified Hagen–Poiseuille law was used, given by $(Q = \Delta P/R_H)$, where Q is the flow rate, ΔP is the applied pressure and R_H is the hydrodynamic resistance.[35] The relative (above or below ambient pressure) pressures $\Delta P_{Leg\ 1}$ and $\Delta P_{Leg\ 2}$ applied by the pressure controller on the reservoir were simulated as voltage sources. They instigate fluid flow in the channels. The hydrodynamic resistance of the entire fluidic system was obtained by splitting the geometry into individual parts and combining them into a single formula according to an electrical resistor network (see ESI: sections 3,4 and 5†). The resistances of the tubing from the pressure controller to the fluidic interface and the fluidic interface between the tubing and the on-chip reservoir were neglected, since the contributions were at least 2 orders of magnitude lower than the fluidic resistances of the microfluidic channels of the device. The complete hydrodynamic resistance model of the two-channel cantilever chip is given in ESI section 5.† Since a steady state, convection-only, single-phase (only liquid) model was considered, no hydrodynamic capacitance, surface tension or diffusion was included in the network analysis. The equations to obtain the flow rate in the channels are eqn (5)–(7).

$$Q_{Leg\ 1} = (\alpha)\Delta P_{Leg\ 1} + (\beta)\Delta P_{Leg\ 2} \tag{5}$$

$$Q_{Leg\ 2} = (\kappa)\Delta P_{Leg\ 1} + (\gamma)\Delta P_{Leg\ 2} \tag{6}$$

$$Q_A = Q_{Leg\ 1} + Q_{Leg\ 2} \tag{7}$$

where, $Q_{Leg\ 1}$, $Q_{Leg\ 2}$ and Q_A are flow rates in Leg 1, Leg 2 and through the aperture respectively in pl s^{-1}. $\Delta P_{Leg\ 1}$ and $\Delta P_{Leg\ 2}$ are applied pressures at the controller on the respective legs in mbar. Due to the symmetry in the device, the coefficients $\alpha = \gamma$ and $\beta = \kappa$ in eqn (5) and (6). They are found to be 0.119 pl (mbar s)$^{-1}$ and −0.047 pl (mbar s)$^{-1}$ respectively for our device (see ESI Table S1,† for detailed calculations). A negative value in the flow rate indicates fluid flow towards the reservoir.

3.2.2. Concentration distribution. The transport of solutes is not only controlled by convection but also by diffusion. The dimensionless mass transfer number Peclet[36] indicates which one of the two, between convective flow or diffusive flow, dominates.

$$P_e = \frac{Ul}{D_m}, \tag{8}$$

for which U is the characteristic velocity of the system (m s^{-1}), l is the characteristic length scale (m) and D_m is the molecular diffusion coefficient (m^2 s^{-1}). For $P_e > 1$ convective and for $P_e < 1$ diffusive flow dominates. For a pressure-driven flow, the parabolic axial velocity profile causes dissolved molecules to spread along the axial (flow) direction of the channel. This

hydrodynamic dispersion[37] effect increases the effective diffusion, D_{eff}, of the system.[38] For conditions where $P_e \ll L/h$:

$$D_{eff} = D_m\left(1 + \frac{A}{192}P_e^2\right), \tag{9}$$

where L is the channel length (m), h is the channel height and A is a constant determined by the cross-sectional shape of the microfluidic channel. A is independent of the flow rate, fluid properties and absolute channel sizes[38,39]

$$A = \frac{96}{105}\left(1.759 + \frac{(7.951 - 1.759)(R - 1)^2}{(R - 0.1)^2}\right), \tag{10}$$

with $R = w/h$, the width-to-height ratio of the microfluidic channel. When transporting plugs of different liquids inside a microchannel, hydrodynamic dispersion can lead to widening of the interfacial region between two plugs. At the starting situation, concentration $C = C_0$ at $x < 0$, while $C = 0$ at $x > 0$. The broadening of the interface region over time can be obtained through solving the passive scalar convection–diffusion equation[36,40] using the effective diffusion term

$$\frac{\partial C}{\partial t} = D_{eff}\frac{\partial^2 C}{\partial x^2}, \tag{11}$$

$$\frac{C}{C_0} = \frac{1}{2} + \frac{1}{2}\mathrm{erf}\left(\frac{x}{2\sqrt{D_{eff}t}}\right), \quad \text{for } x < 0 \tag{12}$$

$$\frac{C}{C_0} = \frac{1}{2} - \frac{1}{2}\mathrm{erf}\left(\frac{x}{2\sqrt{D_{eff}t}}\right), \quad \text{for } x > 0 \tag{13}$$

The transition length[7] (x_s, in m) is the length over which the concentration varies from fC_0 to $(1 - f)C_0$, with f (a value between 0 and 1) indicating the dilution of the starting concentration C_0. For the time that the liquid is transported inside the microfluidic channel ($t = L/U$ in seconds), the transition length is

$$x_s = 4\sqrt{\frac{D_{eff}L}{U}}\mathrm{erf}^{-1}(1 - 2f). \tag{14}$$

4. Materials and methods

4.1 Chemicals

Fluorescein solution (Sigma-Aldrich, molecular weight = 332.31 g mol^{-1}) was prepared with a concentration of 0.14 g l^{-1} in water or 20 mmol Tris-HCl (pH 7.5), 200 mmol NaCl buffer, depending on the case. All fluorescein solutions were filtered 2 times with 0.1 µm pore size PTFE filters (Puradisc) before use. The rhodamine-labelled liposome solution (1% TRITC-DHPE (Biotium), 69% POPC, 15% DOPA, 15% DOPE (Avanti polar lipids); 0.1 mg ml^{-1} in 20 mmol Tris-HCl (pH 7.5), 200 mmol NaCl buffer) was prepared via dialysis against 20 mmol Tris-HCl (pH 7.5), 200 mmol NaCl. The size distribution was homogenized by extruding the liposome solution through a 100 nm pore-size filter (Avanti mini extruder) for 30 passages.

4.2 Fluidic interface

The fluidic connection to the microfluidic probe-chip was established through a 3D printed plastic interface glued to the chip. The interface had two fluid ports, each separately addressable through a glued stainless steel tube (see ESI Fig. S5†). A Tygon tube was plugged to the stainless tube for fluid flow connection.

4.3 Experimental setup

The setup consists of a probe-chip glued to a fluidic interface, two fluid reservoirs, a pressure controller and an inverted optical microscope for visualization (see ESI Fig. S6†). The devices were used as-fabricated without any further modification, so the silicon nitride surface of the cantilever both inside and outside was mildly hydrophobic. The probe-chip was clamped on the stage of an inverted optical microscope (Axiovert 40 MAT, Zeiss) in such a way that the cantilever can be visualized. The greyscale camera of the microscope (AxioCam MRm, Zeiss) was used to record videos of dynamic events. The microscope used a mercury lamp (HXP 200W, Zeiss), a filter set Zeiss 38 HE, suitable for fluorescein dye and a filter set Zeiss 43, suitable for rhodamine dye. The two channels of the probe were connected to external fluid reservoirs (a syringe tip, Nordson EFD Fluid Dosing System Tips, 32 GA). A volume of 50 µl was loaded into the tips. These tips were connected to their individual pressure channels. A pressure controller (OB1 mk3 from Elveflow) was used to control the pressure. By applying a pressure either above or below ambient pressure on the pressure channels, the fluid could be dosed or aspirated, respectively, through the probe tip apertures. Using the 2 pressure outlet channels of the controller, pressure from 0 to −970 mbar (note that −970 mbar means 970 mbar below ambient pressure) and pressure from 0 to 5000 mbar (above ambient pressure) were applied. The water-based solutions, fluorescein and rhodamine, were chosen to visualise fluid motion through the 2-channel microfluidic AFM cantilevers.

4.4 Data analysis

All experiments were performed at fixed camera settings to ensure that the fluorescence intensity recorded could be compared between different conditions. Fluorescence intensity profiles of fluid manipulations were obtained from the greyscale experimental movies using ImageJ. The movies were loaded as stacks and the regions of interest were marked with either a circle or a line, and then the function plot Z-axis profile was used to obtain the intensity plots. The greyscale movies were assigned fluorescent colours only for visualization purposes.

5   Results and discussion

The two-channel microfluidic AFM cantilever was tested for its performance on pipetting and concentration dosing. To fill the channels, the liquid was injected either through the reservoirs (called here "back-loading") or aspirated through the tip

aperture (called here "front-loading"). A combination of front loading and back-loading was also performed. The results are divided into four case studies, case 1: dosing in air, case 2: dosing in water, case 3: dosing and aspiration in water and case 4: co-dosing in water (concentration dosing). All the tested experimental conditions are given in ESI Table S2.† Before the details of the case studies, the fluidic resistance was analyzed.

5.1 Fluidic resistance

The hydrodynamic resistance in the entire fluidic network of external tubing, on-chip reservoir, on-chip channels, cantilever channel and apertures is analysed using an electrical equivalent (see ESI: section 5, Fig. S7 and S8†). The entire fluidic network was simplified to five resistive elements: on-chip Leg 1, cantilever Leg 1, on-chip Leg 2, cantilever Leg 2 and apertures & pyramid.[35,41,42] Their relative contribution to the total resistance of the probe is given in Fig. 3. The rest of the fluidic resistance, like on-chip reservoir and tubing, are neglected, because their contribution to the total fluidic resistance was minimal. The situation shown in Fig. 3 is for a case, where channel 1 (connected to Leg 1) was pressurized with $\Delta P\_Leg 1$ = 500 mbar and $\Delta P\_Leg 2$ = 0 mbar. The largest resistance of 43.2% comes from the on-chip channel of Leg 1, followed by 26.4% from cantilever Leg 1. Then the resistance offered by channel 2 (cantilever and on-chip channel of Leg 2) was 17.1% and finally that offered by the pyramid and apertures was 11.2%. This indicates that 60% of the fluid coming from channel 1 would flow out through the apertures and 40% of the fluid would flow back into channel 2. For the situation when an equal amount of pressure was applied on both channels, the highest resistance came from the apertures, 40%. The remaining part of the channels offered equal resistance from either side, 30% each. A detailed overview of all the hydrodynamic resistance values is given in ESI Table S1.† In summary, the hydrodynamic resistance of each leg was 6 ×
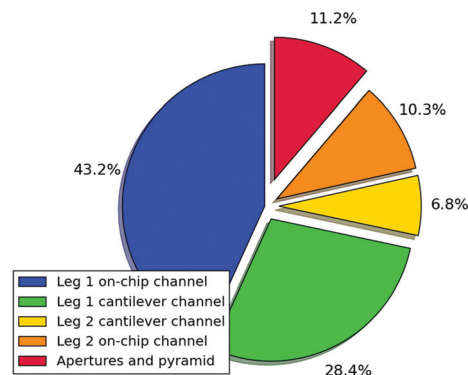
Fig. 3 Pie chart indicating the weighted contribution of various fluidic elements to the overall hydrodynamic resistance of the two-channel microfluidic AFM cantilever. Each microfluidic channel is divided into a cantilever part and an on-chip part (the channel that is on the carrier chip). Here, the contribution of the fluidic components to the total hydrodynamic resistance is shown for $\Delta P\_Leg 1$ = 500 mbar and $\Delta P\_Leg 2$ = 0 mbar.

10^{17} Pa s m^{-3} and that of the pyramid together with the apertures was 3.9×10^{17} Pa s m^{-3}. A single channel microfluidic AFM probe used for dispensing by Grüter *et al.*[43] had a hydrodynamic resistance in the range of 1×10^{18} Pa s m^{-3}. Note that their device dimensions and aperture sizes were different. A movie showing the fluorescein meniscus in the channels as a function of applied pressure for an aperture-clogged cantilever is shown in ESI Movie 3.†

5.2   Case 1: dosing in air

The goal of this study was to understand the dosing of two different types of liquids through the same apertures with air as the outside environment. We expect that a high overpressure is needed to dispense in air. This is due to a large Laplace pressure that needs to be overcome, since the apertures are narrow and the surface tension of the water/air interface is high. However, once the liquid comes out and forms a small droplet near the apertures, the pressure needed to control the flow rate decreases depending on the droplet size and the evaporation rate.[44] This is because, once the surface tension has decreased, the hydrodynamic resistance of the microfluidic channels govern the growth of the droplet.

Two different fluorescent liquids, fluorescein and rhodamine-labelled liposomes, were back-loaded into the microfluidic AFM cantilever. To begin, only one fluidic channel was loaded, while the other fluidic channel was still open to the ambient pressure. This enabled a quick back-loading process of the first liquid, as the air inside the fluidic system was pushed out through the other leg and reservoir. Reservoir 1 was filled with fluorescein by applying $\Delta P\_\mathrm{Leg}\ 1 = 500$ mbar. Then, reservoir 2 was filled with rhodamine-labelled liposomes. An air gap was created between the two liquids during the filling process, which separated the two liquids without mixing. Such air gaps are typically used in microfluidics to keep the reagents separate without mixing.[45] In this situation, the only exit path for both liquids and the trapped air between the liquids was through the tip apertures.

The presence of an air gap separating the two liquids was also confirmed by a higher pressure needed to load the rhodamine-labelled liposomes into the cantilever compared to the fluorescein; $\Delta P\_\mathrm{Leg}\ 2 = 1500$ mbar. The dosing of fluorescein by applying $\Delta P\_\mathrm{Leg}\ 1 = 2000$ mbar is shown in Fig. 4. The green fluorescent signal originated from the fluorescein liquid coming out through the apertures and forming a large droplet on the outside surface of the cantilever (see ESI Movie 4†). Then, by increasing the pressure on Leg 2, $\Delta P\_\mathrm{Leg}\ 2$ to 2100 mbar, rhodamine-labelled liposome solution was dosed. This solution was not as bright as fluorescein, because rhodamine was present only on the membrane of the liposomes. Therefore, the rhodamine molecules were less evenly distributed over the liquid (see ESI Movie 5).†

Switching between the two liquids was slow and difficult to control. High pressures were needed to compress the air between the two liquids, and it took between 10 s to 60 s for the liquid meniscus to reach the cantilever tip. When it
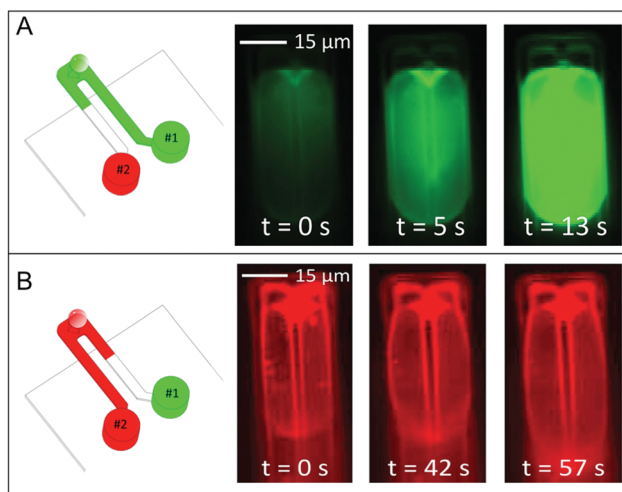

Fig. 4 Dosing two different liquids separated by an air gap inside the channels. (A) Dosing of the fluorescein by applying a pressure of $\Delta P\_\mathrm{Leg}\ 1 = 2000$ mbar on the reservoir filled with the liquid. The dosed liquid through the aperture and occupying the cantilever surface outside after 5 s and 13 s of liquid exiting through the channel is shown. (B) Dosing of rhodamine-labelled vesicles by applying a pressure of $\Delta P\_\mathrm{Leg}\ 2 = 2100$ mbar on the corresponding reservoir.

arrived, the speed of the liquid meniscus was high, making it difficult to manipulate small liquid volumes.

Simulations of two-phase (water and air) are computationally intensive. However, we did simulate the cantilever filling process (see ESI Movie 2).†

5.3.   Case 2: dosing in water

The goal of this study was to understand the dosing rate control in water. In this experiment, only reservoir 1 was filled with fluorescein and reservoir 2 was kept empty without any liquid. The fluorescein was dosed in deionized water through the tip apertures, see Fig. 5A. The experiments were performed in which $\Delta P\_\mathrm{Leg}\ 1$ was set to 10, 20, 30, 40, 50, 100, 200 or 500 mbar, while $\Delta P\_\mathrm{Leg}\ 2$ was kept at atmospheric pressure, $\Delta P\_\mathrm{Leg}\ 2 = 0$. We expect the flow rate and concentration of the dosed liquid to increase with pressure. Apart from diffusion, the dosed amount of the fluid and its concentration due to convection depends on the fluidic resistance of the aperture. As the two channels are connected, some fluid from channel 1 will also enter into channel 2. The amount depends on the ratio of the pressure applied on Leg 1 and Leg 2.

From the analytical model, the flow rate through the apertures was obtained for the entire pressure span on both reservoirs: Fig. 5B. The cross-marks represent the conditions for which experiments were performed. The flow rate through the apertures ranged from 0.72 to 36 pl s^{-1}.

When the fluorescein-filled cantilever was kept in water without applying any pressure, water diffuses into the fluorescein-filled channels and fluorescein diffuses into the surrounding through the aperture and reaches a quasi-static equilibrium in the cantilever channel. In this quasi-static equilibrium, fluorescein inside Leg 1 will be about 60% diluted in
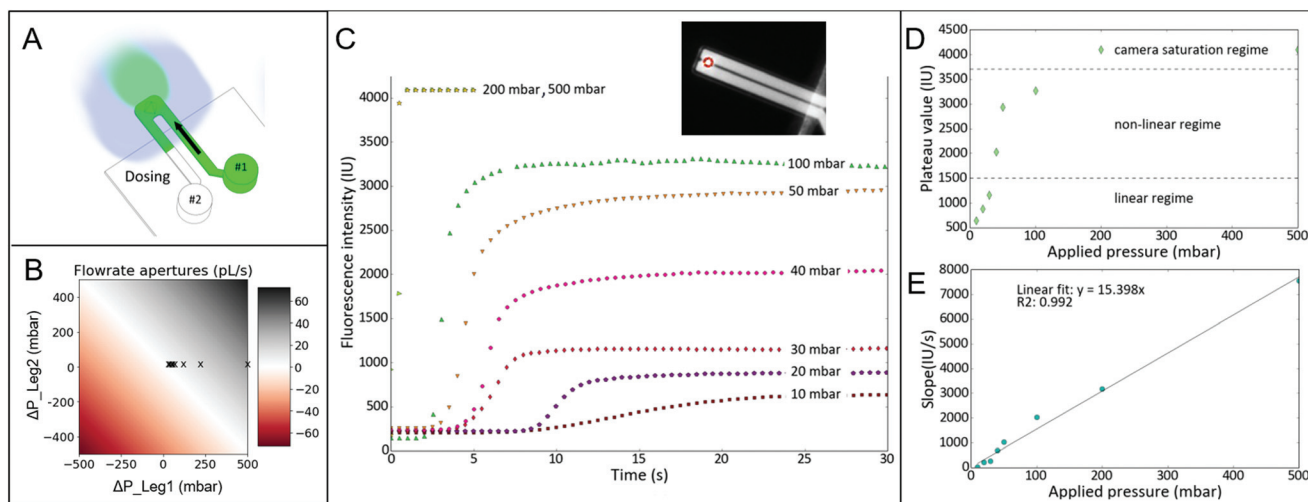
Fig. 5 Dosing of fluorescein. (A) Schematic of experiment where fluorescein solution was dosed from Leg 1 into water (case 2). (B) A map of the fluid flow rate through the apertures obtained from the analytical equations. The crosses indicate the experimental conditions tested. (C) Graph obtained of the averaged fluorescence intensity while pressurizing reservoir 1 (containing fluorescein) at the mentioned pressures for 30 s. In the case of the applied overpressures 200 mbar and 500 mbar, the pressure was only applied for 5 s and around 4100 IU the camera was saturated. The inset shows the averaged fluorescein intensity measured at a 12 × 12 pixel region close to the cantilever tip (indicated by a red circle). (D) The average intensity of the plateau for every applied pressure extracted from the graph of (C), divided into 3 regimes. (E) The extracted slope of the linear region during the fluorescent increase of the graph of (C).

concentration compared to the fluorescein in the reservoir (confirmed from simulations). This 60% forms the baseline for the fluorescence intensity at the tip defining time $t = 0$ s for dosing measurements. The fluorescence intensity, at a location indicated by a circle near the tip (inset Fig. 5C), is plotted in Fig. 5C. It was obtained from movies recorded for different applied pressures. The steepest slopes represent the maximum fluid flow rate and plateaus represent the new concentration (between 60% and 100% of fluorescein). The fluorescence intensity around the tip for all applied pressures started approximately at the same base level (steady state baseline). Then, for different applied pressures on reservoir 1, the fluorescent signal started to increase and reached a plateau. The starting time point of increase in the fluorescent signal varied; the higher the applied pressure, the higher was the increase in the fluorescence intensity, and the higher was the value where the signal reached a plateau.

The plateau values of the fluorescein intensity in Fig. 5C are plotted in Fig. 5D. Until 100 mbar, the intensity signal increases and saturates at a lower value than the maximum possible intensity. It indicates that, as the applied pressure increases, the convective flow starts to increase over diffusive flow, proportional to the applied pressure. Then for 200 mbar and 500 mbar, the intensity saturates at a maximum possible value the maximum possible value from the camera.

The slope of the intensity curves for different pressures in Fig. 5C is plotted in Fig. 5E. This plot is a good representation of the flow rate through the apertures. The slope of this plot indicates that the flow rate is linear with applied pressure, indicating that the resultant flow satisfies the Hagen–Poiseuille pressure-driven flow.[35] With these experiments, it is difficult to measure the dosed volume, because the volume

dosed into the "open" (outside the cantilever) is not confined. By monitoring the intensity change in different frames over the length of the channel, and knowing the channel dimensions, the flow rate was deduced and is given in Table 2. A negative value of the flow rate indicates that the fluid is flowing towards the reservoir. The error given is 2× standard deviation obtained during the data analysis, when interpreting the centre of the moving (diffused) fluorescence intensity profile. Measurements were only for 30 mbar and 50 mbar, otherwise, the frame rate of the camera was too slow. When comparing the measured flowrates to the flowrates derived from the analytical model, the flowrates from Leg 1 match very well, while the rates obtained from Leg 2 only give an indication of the correct order. This can be explained by the sensitivity of the measurement method to diffusion. As low flow rates become more diffusion-dominated, the transition length increases over time. This makes it more difficult to correctly trace the movement of the fluorescence boundary over time and leads to an over-estimation of the flowrate in Leg 2 of

Table 2 Flowrates measured inside the channels during dosing (case 2) by tracking the center of the diffused boundary between water and fluorescein. The pressure applied at the fluidic reservoirs is given. Here $\Delta P_{Leg\,2} = 0$ mbar was fixed. The error is the uncertainty in determining the position of $0.5 \times I_{max}$ value. The units of applied pressure difference $\Delta P_{Leg\,1}$ and flow rate Q at different locations are in mbar and pl s^{-1} respectively

	Experiment			Analytical		
$\Delta P_{Leg\,1}$	$Q_{Leg\,1}$	$Q_{Leg\,2}$	Q_A	$Q_{Leg\,1}$	$Q_{Leg\,2}$	Q_A
30	4.14 ± 0.3	-3.4 ± 0.1	NA	3.57	−1.41	2.16
50	6.25 ± 0.1	-4.29 ± 0.1	NA	5.95	−2.35	3.60

about 50%. Additional data on dosing is given in ESI Movie 6, Fig. S9 and S10.†

5.4 Case 3: aspiration in water

The goal of this study was to understand the loading of the outside liquid into the microfluidic AFM cantilever from the tip apertures. In this experiment, the surrounding water was aspirated into Leg 2 that was already filled with fluorescein. The motion of the diffused boundary between water and fluorescein during aspiration was monitored and analyzed for the flow rate. Numerical simulations were performed to understand the flow and concentration profile near the pyramid and channels.

Initially both channels of the microfluidic cantilever were filled (by back-loading) with fluorescein solution through Leg 1. Then, deionized water was aspirated (front-loading) into Leg 2, see Fig. 6A. The pressure for aspiration ($\Delta P\_Leg 2$) was set at −10 mbar. Note that such negative values for pressure means below atmospheric pressure. Leg 1 was kept at atmospheric pressure during the water aspiration. In order to verify that the fluorescein of Leg 2 would be replaced by water upon aspiration, the fluorescence intensities in the Leg 2 cantilever channel and on-chip channel were monitored as a function of time. As Leg 1 was also connected to the tip apertures through the small pyramid near the tip (see Fig. 2c), we expect that both water from outside and fluorescein from channel 1 will
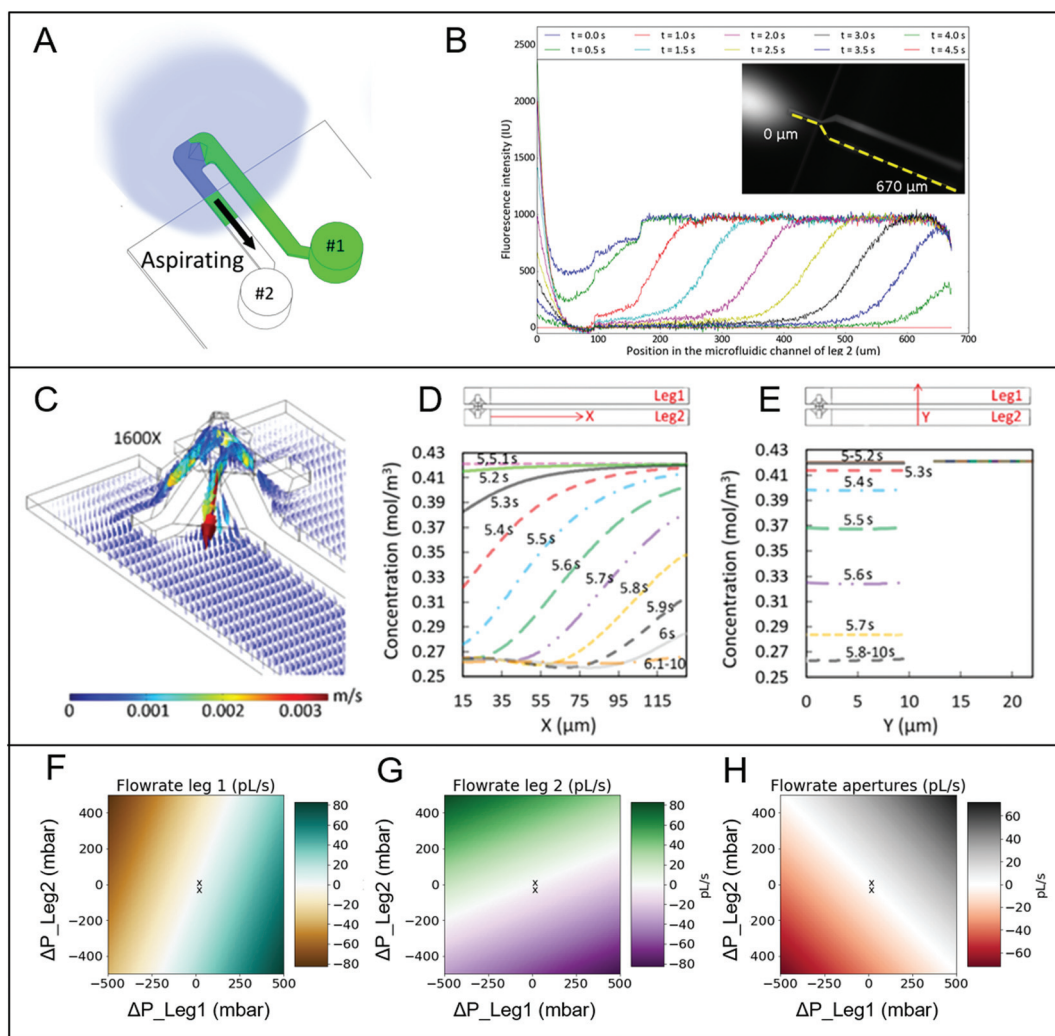

Fig. 6 Aspiration of water. (A) Inset 1: Schematic of the cantilever while aspirating water into a cantilever filled with fluorescein solution. (B) Fluorescence intensity profile of Leg 2 for $\Delta P\_Leg 1 = 0$ mbar and $\Delta P\_Leg 2 = −10$ mbar with time. The inset shows a snapshot taken during the ImageJ analysis of the intensity along the indicated dashed line; 0 μm is close to the cantilever tip, while 670 μm is in the on-chip part of the channel. Prior to water aspiration, the cantilever was filled with fluorescein solution, which is responsible for the huge intensity signal near the tip. (C–E) Numerical simulation results for $\Delta P\_Leg 1 = 0$ mbar and $\Delta P\_Leg 2 = −10$ mbar. (C) Fluid flow velocity profile inside the cantilever and tip channels. The arrows indicate the flow direction. The value 1600× represents the magnified value of the vectors shown. (D) Concentration profile inside the cantilever along the length (x-direction) in Leg 2. Note that the total length of the cantilever channel is 121 μm. (E) Concentration profile inside the cantilever along breadth (y-direction) in both legs. (F–H) Analytically calculated flow rate map in Leg 1, Leg 2 and at the apertures respectively for different applied pressures on the reservoirs. The crosses indicate the experimental conditions tested.

be aspirated into channel 2. The amount of water and fluorescein aspirated depends on their respective fluidic resistances and the ratio of applied pressures. Therefore, it is also expected that channel 2 will have diluted fluorescein concentration and not just water.

The fluorescence intensity plot of Leg 2 is shown in Fig. 6B. The x-axis shows the position where the fluorescence intensity was measured along the channel; 0 µm is close to the cantilever tip and 670 µm is the last visible location of the on-chip fluidic channel (note that the length of the cantilever leg was 121 µm). Near the tip of the cantilever a large fluorescent signal was observed, which originates from dosing of the fluorescein into the water outside while filling Legs 1 and 2. This led to an increased intensity signal between 0 µm and 50 µm in the plot. Between 180 µm–670 µm, the fluorescence intensity decreased over the channel length with time, indicating that the water solution was aspirated into Leg 2. It took about 4.5 s to fill the visible part of the channel with water for −10 mbar of applied pressure on Leg 2. The flow rate obtained from the experimental data is shown in Table 3. Additional experimental and simulation data for aspiration is shown in ESI Fig. S11 and Movie 7.† The experimental data processing procedure is also described in ESI section 8.†

The fluid flow inside the cantilever (only 121 µm long) was numerically simulated for the applied pressure of −10 mbar to reservoir 1. Note that the pressure applied to a reservoir is not the same as the pressure inside the cantilever channel. After trial and error in matching the experimental flow rate in the channel, it was found that there was a 60% loss in the pressure from the pressure applied at the pressure controller and the pressure at the cantilever. Note that the analytical equations predicted a 53.5% pressure loss over the on-chip channels. This indicates that the numerical simulations slightly over-estimate the hydrodynamic resistance of the microfluidic channels not included in the simulations. This explains why the simulated flowrates slightly differ from the analytically-determined values. The simulated flow profile inside the cantilever is shown in Fig. 6C. The maximum velocity of the fluid, 3 mm s^{-1}, is obtained near the narrow fluid channels before the pyramid.

Next, the concentration profile inside the cantilever was analyzed by simulations. The concentration profile of fluorescein along the cantilever length in Leg 2 and is given in

Fig. 6D. The convective motion of the plug at different times within 1 s is shown. The slopes of the profile lines at various times seems to be constant, indicating the convective flow of the diffused plug. The concentration of fluorescein drops to 60% of the maximum (from 0.420 mol m^{-3} to 0.252 mol m^{-3}). The concentration profile of fluorescein along the cantilever width at different time points in Leg 1 and Leg 2 is given in Fig. 6E. Over the cantilever width of Leg 2, the concentration of the fluorescein is uniform. The concentration in Leg 1 did not change and always remained high, because it was connected to fluorescein reservoir 1. It also indicates that during the initial 10 s of applying −10 mbar on reservoir 2 and 0 mbar pressure on reservoir 1, there was no dilution of the fluorescein concentration up to 65 µm (the monitoring position) of Leg 2.

The flow rates calculated analytically in Leg 1, Leg 2 and the apertures for the entire pressure span on reservoir 1 and reservoir 2 are shown in Fig. 6F, G and H respectively. Both apertures were treated as connected in parallel from the perspective of fluidic resistance and hence the equivalent of the parallel was analyzed/plotted for the common fluid outflow. The cross-marks represent the pressure values (ΔP_Leg 1 = 0 mbar and ΔP_Leg 2 = −10 mbar, −50 mbar) where the experiments were performed. The experimental data for −50 mbar is in ESI Fig. S10.† When comparing the flow rates measured from the experiments (Table 3) to the analytically-derived values, the flowrate of the lowest under pressure condition matched less with the analytical model. As explained in section 5.3, the flowrate measurement is less accurate at low peclet values (diffusion-dominated flows).

5.5   Case 4: co-dosing in liquid—concentration dosing

The goal of this study was to understand simultaneous dispensing of two different liquids in a liquid environment. Besides dosing and aspirating one type of liquid, the two-channel microfluidic AFM cantilever can also dose a mixture of two liquids, which allows dosing different concentrations of liquid in a given volume. By controlling the applied pressure on both legs, the fluid volume and the analyte concentration flowing-out through the aperture can be tuned.

For this experiment, Leg 1 was filled with fluorescein solution (through back-loading) and Leg 2 with water by aspiration from the outside medium. Then the applied pressures on reservoirs 1 and 2 were altered (Fig. 7A). The flow rate and the concentration dosed through the apertures were calculated analytically for the entire range of applied pressures, and are given in Fig. 7B and C respectively.

Co-dispensing for three different conditions is shown in Fig. 7D–F. Every image is a frame from a recorded movie. The corresponding pressure values applied on Leg 1 and Leg 2 are given on the top right-side and bottom right-side of the channels respectively. At frame t = 0 s water is aspirated into Leg 2. The frames taken from t = 1 s to 4 s display various co-dosing situations. Leg 2 was filled with water and ΔP_Leg 2 was kept at 200 mbar for all experimental conditions. Leg 1 was filled with fluorescein solution and ΔP_Leg 1 was varied by 50, 80

Table 3 Flowrates measured inside the channels during aspiration (case 3) by tracking the centre of the diffused boundary between water and fluorescein. The pressure applied on fluid reservoir 2 is given. Here $\Delta P_{Leg\ 1}$ = 0 mbar was fixed. The error is the uncertainty in determining the position of $0.5 \times I_{max}$ value. The units of applied pressure difference $\Delta P_{Leg\ 2}$ and flow rate Q at different locations are in mbar and pl s^{-1} respectively

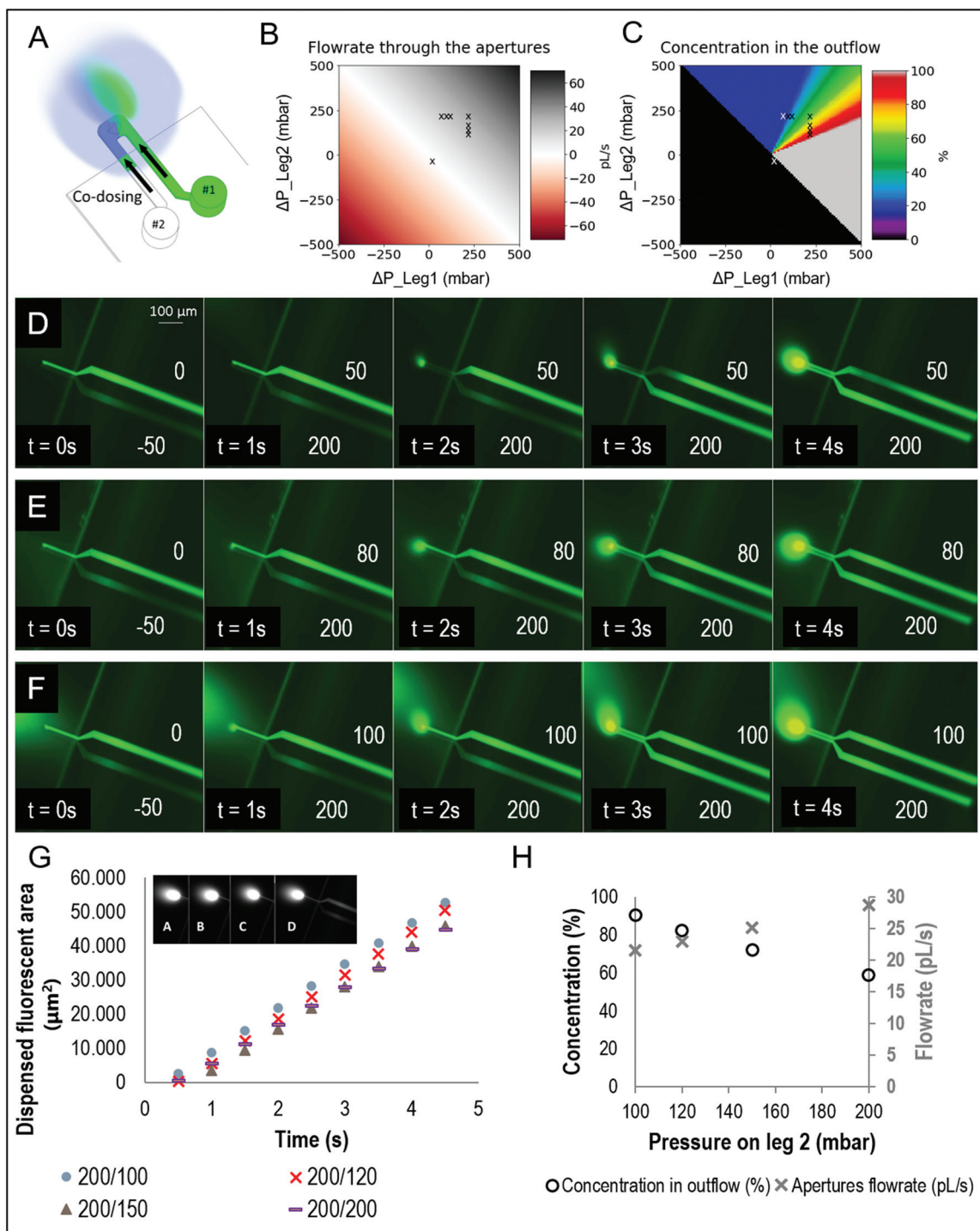|	Experiment			Analytical		
$\Delta P_{Leg\ 2}$	$Q_{Leg\ 1}$	$Q_{Leg\ 2}$	Q_A	$Q_{Leg\ 1}$	$Q_{Leg\ 2}$	Q_A
−10	NA	−4.08 ± 0.0	NA	0.47	−1.19	−0.72
−50	NA	−8.96 ± 0.1	NA	2.35	−5.95	−3.60

Fig. 7 (A) Schematic of co-dosing of water and fluorescein. (B) Fluid flow rate map analytically calculated for various applied pressures with crosses indicating the experimental conditions tested. (C) Concentration of the liquid dosed for various applied pressures with crosses indicating the experimental conditions tested. (D–F) Fluorescence images of the controlled dosing of liquids at different concentrations. At $t = 0$ s, water is aspirated into Leg 2 by applying $\Delta P\_Leg 1 = 0$ mbar pressure, while $\Delta P\_Leg 2 = -50$ mbar. Then, starting from $t = 1$ s, Leg 1 with fluorescein solution was tuned through different pressure conditions for dosing: (D) $\Delta P\_Leg 1 = 50$ mbar, $\Delta P\_Leg 2 = 200$ mbar. (E) $aP\_Leg 1 = 80$ mbar, $\Delta P\_Leg 2 = 200$ mbar. (F) $\Delta P\_Leg 1 = 100$ mbar, $\Delta P\_Leg 2 = 200$ mbar. (G) Measured dispensed fluorescence area when the channel with water solution was tuned through different pressure conditions for dosing taken at $t = 3.5$ s, inset (A) $\Delta P\_Leg 1 = 200$ mbar, $\Delta P\_Leg 2 = 100$ mbar, inset (B) $\Delta P\_Leg 1 = 200$ mbar, $\Delta P\_Leg 2 = 120$ mbar, inset (C) $\Delta P\_Leg 1 = 200$ mbar, $\Delta P\_Leg 2 = 150$ mbar, inset (D) $\Delta P\_Leg 1 = 200$ mbar, $\Delta P\_Leg 2 = 200$ mbar. (H) Concentration and flowrate of the dosed liquid calculated using the analytical model, for conditions mentioned in G.

and 100 mbar respectively. See ESI Movie 8† for the case shown in Fig. (7E).

For $\Delta P\_\text{Leg 1} = 50$ mbar, Fig. 7D shows a gradual increase of the fluorescence signal at the outlet (see $t = 1$ s and 4 s). For $\Delta P\_\text{Leg 1} = 80$ mbar, Fig. 7E shows a similar behaviour. However, the intensity of fluorescence was higher than the previous condition with time. For $\Delta P\_\text{Leg 1} = 100$ mbar, Fig. 7F shows again a similar behaviour but displaying an even higher intensity. Note that the increased intensity of the fluorescent signal alone is not indicative of concentration dosing, because the volume of the dosed liquid also increases with increasing pressure applied to Leg 1 (with fluorescein). Therefore the increase in fluorescence intensity should be carefully interpreted in terms of concentration and volume.

To disentangle this information, we use the analytical plots shown in Fig. 7B and C. The three horizontal cross-marks in the plots indicate these experimental cases. The black right-angled triangle region in Fig. 7C indicates the region where dosing of the liquid through the apertures is impossible, and there will be aspiration through the apertures for those settings of pressure. The grey coloured area on the right-side is where the pressure in Leg 1 (filled with fluorescein) dominates, without any control on the concentration dosing. The blue coloured area on the top-side of the figure is where the pressure on Leg 2 (filled with water) dominates, again without any control on the concentration dosing. The concentration value of this blue region was defined by the molecular diffusion of fluorescein in water. The region with a spread of colours indicates where concentration dosing is possible. The three cross-marks on the $\Delta P\_\text{Leg 2} = 200$ mbar line for three experimental cases (Fig. 7D–F) in both Fig. 7B and C indicate that the flow rate for experimental conditions was between 18 and 22 pl s^{-1} and the concentration was between 17.5 and 27%.

For co-dosing experiments, as there was no clearly discernible boundary between water and fluorescein inside the channels, it was not possible to determine the flow rate by experiments, therefore, the values calculated analytically are given in Table 4. When comparing the experimental stills taken at $t = 4$ s shown in Fig. 7D–F, it is visible that the fluorescence area outside the apertures becomes larger while the pressure on Leg 1 is increased from 50 to 100 mbar. This fits well with the analytically calculated increase of the concentration in the outflow shown in Table 4.

Table 4 Flowrate comparison obtained by the analytical model for case 4. All pressures are applied at the fluidic reservoir with $\Delta P_{\text{Leg 2}} = 200$ mbar in Fig. 7D–F. The units of applied pressure difference $\Delta P_{\text{Leg 1}}$, flow rate Q at different locations and concentration through aperture C_A are in mbar, pl s^{-1} and percentage (%) respectively

$\Delta P_{\text{Leg 1}}$	Analytical				
	$Q_{\text{Leg 1}}$	$Q_{\text{Leg 2}}$	Q_A	$Q_{\text{Leg 1}}/Q_A$	C_A (C/C_0)
50	−3.5	21.5	18.0	−0.194	17.5
80	0.1	20.1	20.2	0.004	18.0
100	2.5	19.1	21.6	0.114	27.0

In another set of experiments, the pressure on Leg 1 (filled with fluorescein) was kept constant (200 mbar) and the pressure on Leg 2 (filled with water) was varied (100, 120, 150 and 200 mbar). The dosed fluorescence equal intensity area for these conditions is plotted in Fig. 7G. The plot shows the area measured in every recorded movie exactly at the same time ($t = 3.5$ s) after dosing was performed, for all the tested pressure conditions. The equal intensity area decreases with increasing pressure on Leg 2 (water) which indicates that less fluorescein was dispensed. The quantitative values taken from the analytical model (the experimental conditions are marked as vertical crosses in the maps of Fig. 7B and C) are shown in Fig. 7H with dosed concentration on the left y-axis and flow rate on the right y-axis. Fig. 7H shows that when the pressure on Leg 2 is increased, the flowrate increases, but the concentration of fluorescein in the outflow decreases. The flow rates changed from 22 to 29 pL s^{-1} and the concentration changed from 90% to 59%. By multiplying the flowrate with the concentration dispensed, it is found that the amount of fluorescein dispensed per second decreases when the pressure on Leg 2 increases. This confirms the trend visible in the experimental data of Fig. 7G: even with a higher flowrate, less fluorescein is dispensed because the concentration in the outflow is tuned to be lower.

By using the analytically derived flow rate and concentration in the outflow maps given in Fig. 7B and C, respectively, pressure values can be identified to obtain the desired flowrate and concentration values for future experiments.

5.6 Transition length

At the boundary between water and fluorescein, molecular diffusion between the two solutions will lead to a dispersion of fluorescein concentration over a length characterized as transition length. In a pressure driven system (Poiseuille flow), the transition length is described by Taylor–Aris dispersion.[36] The molecular diffusion-dependent dispersion D_m is influenced by a pressure driven flow, leading to an effective diffusion D_{eff}, given by eqn (9), which in turn effects the transition length, given by eqn (14). The transition length was calculated for the entire possible pressure range used on the set-up and visualized into a 2D map (Fig. 8A). The transition length was calculated using an f-value of 0.1 and using the time for the flow to move through the entire visible microfluidic channel for one leg, which is 947 μm (this includes both the cantilever and the visible on-chip channel). The cross-marks in Fig. 8A indicate the tested experimental co-dosing conditions in Fig. 7. The plot puts the transition length and the cantilever channel length in perspective as the plot is zoomed-in to all values that lie below 242 μm, which is twice the length of the cantilever channel. A full scale version of the graph can be found in Fig. S12B of the ESI.† For a pressure condition where the flow through the apertures is the lowest (10 mbar, 0 mbar), resulting in a low flow rate of 1.2 pL s^{-1} in Leg 1, there is a transition length of 386 μm, covering the cantilever channel several times. For a maximum difference of applied pressures (500 mbar, −500 mbar), a
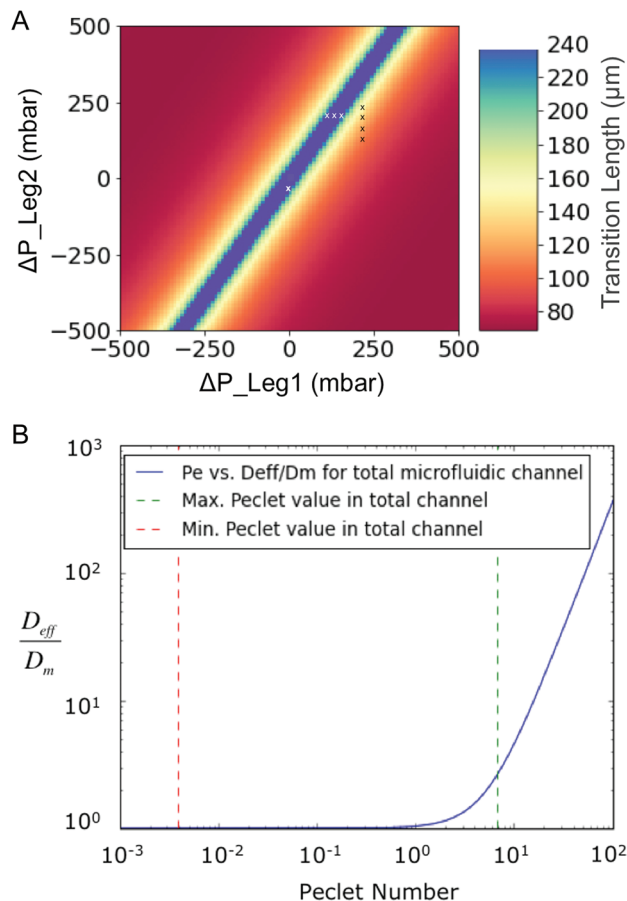
Fig. 8 (A) A map of the transition length for the entire pressure parameter space. The eight experimental tested conditions are marked with crosses. B. The influence of dispersion with Péclet number. The minimum and maximum Péclet number for the device are marked in dashed red and green lines.

transition length of 69 μm is calculated, which is about half of the cantilever channel.

When comparing the zoomed-in map of Fig. 8A to the full scale map of Fig. S12A,† it can be observed that only the very lowest flowrate conditions (which are all arranged on a line through the (0,0)-point) give rise to the highest transition lengths. The maximum transition length is 4214 μm, found at the pressure condition $\Delta P\_Leg\ 1 = -150$ mbar, $\Delta P\_Leg\ 2 = -380$ mbar, when the flow in Leg 1 is only 10 fL s^{-1}. Therefore, it is important to choose experimental conditions that do not lie on this line where the flowrate is almost zero, as the transition lengths become very high.

To understand the influence of dispersion relative to the molecular diffusion of fluorescein in water, their ratio is plotted for various Péclet numbers in Fig. 8B. The maximum and minimum Péclet numbers possible for the device are also marked in the figure. At higher Péclet numbers, the hydrodynamic dispersion increases the effective diffusion and at lower Péclet numbers diffusion is dominated by molecular diffusion. Since the Péclet number stays below 6 in the entire pressure parameter space (−500 mbar to 500 mbar), mostly molecular

diffusion dominates over the effective diffusion value. As a conclusion, to cover a large concentration range when dosing fixed volumes, it is preferred to use high pressures (and high flowrates) for shorter amounts of time compared to low pressures for a longer time in order to minimize dispersion.

6 Conclusions

A two-channel microfluidic AFM cantilever probe was fabricated. The probe has the capabilities of conventional AFM-based imaging. Additionally, the microfluidic cantilever channel with apertures at the tip also enables the dosing of fluids. The two channels of the cantilever were connected to two separate reservoirs. The cantilever channels can be loaded with the liquid either from the reservoir (back-loading) or by aspirating the liquid through the apertures (front-loading). An analytical model for fluidic resistance based on the electrical equivalent and a transition length profile based on Taylor–Aris dispersion were derived. From the models, it was shown that the microfluidic channels (both the on-chip channels and the suspended cantilever channels) offered 88.8% of the total fluidic resistance and the remaining 11.2% came from the apertures and the tip pyramid. Detailed flow and concentration profiles through the channels and apertures were numerically simulated.

Different case studies of dosing and aspiration through the apertures on the cantilever tip were made by front-loading and back-loading. To each reservoir, pressures in the range of −500 mbar to 500 mbar relative to ambient pressure were applied and the effect on the liquid contained in the channels and around the volume outside of the aperture were studied. The maximum and minimum measurable flow rate that was achieved through one of the channels was 83 pl s^{-1} and 10 fl s^{-1} respectively. The smallest dosing flow rate from the apertures was 720 fl s^{-1} with 10 mbar on one reservoir and ambient pressure on the other. A complete flow rate profile map inside each channel and through the apertures was plotted for various pressures applied to the reservoirs. Experiments with fluorescein concentration between 17.5% and 90% of the reservoir value were performed. A complete concentration dosing profile map for different applied pressures was also plotted. This map can be used to determine future experimental parameters to obtain the desired volume and concentration values.

Overall, dosing small volumes of two different liquids separately and simultaneously in a controlled (flow rate and concentration) manner in an "open" microfluidics configuration is shown. The feature being a part of an atomic force microscopy cantilever gives unprecedented opportunity to simultaneously measure atomic forces and manipulate concentrations ranging from femtolitre to picolitre volumes of the fluid. As an example, this capability will enable dosing different concentrations of analytes inside a living cell and mapping the shape and stiffness of the cell with the same probe. As an extension, the probes could be made of multiple

separated channels to accommodate experiments with more liquids.

Author contribution

AHE, US, MKG and ES conceptualised the probes. ES designed and fabricated the probes. AHE, US, MKG and EJV designed the experiments. EJV and MM performed the experiments. MM performed simulations. EJV developed the analytical models and analysed the experimental data. All authors discussed all the data. EJV wrote the initial manuscript, MM wrote the simulation part. MKG and EJV adapted the final manuscript. AHE, US and MKG arranged the funding. All authors commented on and contributed to the revised manuscript.

Conflicts of interest

There are no conflicts to declare.

Acknowledgements

References

1 R. Waasdorp, O. van den Heuvel, F. Versluis, B. Hajee and M. K. Ghatkesar, *RSC Adv.*, 2018, **8**, 14765–14774.

2 A. F. Sartori, P. Belardinelli, R. J. Dolleman, P. G. Steeneken, M. K. Ghatkesar and J. G. Buijnsters, *Small*, 2019, **15**, 1803774.

3 M. S. Hasenbank, T. Edwards, E. Fu, R. Garzon, T. F. Kosar, M. Look, A. Mashadi-Hossein and P. Yager, *Anal. Chim. Acta*, 2008, **611**, 80–88.

4 A. Osterle, *Pipette Cookbook 2018*, Sutter Insturment Company, 2011.

5 D. Juncker, H. Schmid and E. Delamarche, *Nat. Mater.*, 2005, **4**, 622.

6 D. P. Taylor, I. Zeaf, R. D. Lovchik and G. V. Kaigala, *Langmuir*, 2016, **32**, 10537–10544.

7 N. Ostromohov, M. Bercovici and G. Kaigala, *Lab Chip*, 2016, **16**, 3015–3023.

8 A. Kashyap, A. F. Khartchenko, P. Pati, M. Gabrani, P. Schraml and G. V. Kaigala, *Nat. Biomed. Eng.*, 2019, **3**, 478.

9 E. Delamarche and G. V. Kaigala, *Open-space microfluidics: concepts, implementations, applications*, John Wiley & Sons, 2018.

10 S. Mao, C. Sato, Y. Suzuki, J. Yang, H. Zeng, H. Nakajima, M. Yang, J.-M. Lin and K. Uchiyama, *ChemPhysChem*, 2016, **17**, 3155–3159.

11 S. Mao, Y. Zhang, W. Zhang, H. Zeng, H. Nakajima, J.-M. Lin and K. Uchiyama, *ChemPhysChem*, 2017, **18**, 2357–2363.

12 S. Mao, Y. Zhang, Q. Zhang, J.-M. Lin and K. Uchiyama, *Talanta*, 2018, **187**, 246–251.

13 A. A. Kim, K. Kustanovich, D. Baratian, A. Ainla, M. Shaali, G. Jeffries and A. Jesorka, *Biomicrofluidics*, 2017, **11**, 014112.

14 A. Bruckbauer, D. Zhou, L. Ying, Y. E. Korchev, C. Abell and D. Klenerman, *J. Am. Chem. Soc.*, 2003, **125**, 9834–9839.

15 D. Momotenko, A. Page, M. Adobes-Vidal and P. R. Unwin, *ACS Nano*, 2016, **10**, 8871–8878.

16 A. Page, M. Kang, A. Armitstead, D. Perry and P. R. Unwin, *Anal. Chem.*, 2017, **89**, 3021–3028.

17 D. Perry, A. Page, B. Chen, B. G. Frenguelli and P. R. Unwin, *Anal. Chem.*, 2017, **89**, 12458–12465.

18 Y. Gao, B. Li, R. Singhal, A. Fontecchio, B. Pelleg, Z. Orynbayeva, Y. Gogotsi and G. Friedman, *Beilstein J. Nanotechnol.*, 2018, **9**, 850–860.

19 O. Feinerman and E. Moses, *J. Neurosci. Methods*, 2003, **127**, 75–84.

20 A. Meister, M. Gabi, P. Behr, P. Studer, J. Vörös, P. Niedermann, J. Bitterli, J. Polesel-Maris, M. Liley, H. Heinzelmann, *et al.*, *Nano Lett.*, 2009, **9**, 2501–2507.

21 T. Shibata, K. Nakamura, S. Horiike, M. Nagai, T. Kawashima, T. Mineta and E. Makino, *Microelectron. Eng.*, 2013, **111**, 325–331.

22 M. K. Ghatkesar, H. H. P. Garza and U. Staufer, *Microelectron. Eng.*, 2014, **124**, 22–25.

23 K.-H. Kim, N. Moldovan and H. D. Espinosa, *Small*, 2005, **1**, 632–635.

24 O. Guillaume-Gentil, E. Potthoff, D. Ossola, P. Dörig, T. Zambelli and J. A. Vorholt, *Small*, 2013, **9**, 1904–1907.

25 O. Guillaume-Gentil, R. V. Grindberg, R. Kooger, L. Dorwling-Carter, V. Martinez, D. Ossola, M. Pilhofer, T. Zambelli and J. A. Vorholt, *Cell*, 2016, **166**, 506–516.

26 O. Loh, R. Lam, M. Chen, N. Moldovan, H. Huang, D. Ho and H. D. Espinosa, *Small*, 2009, **5**, 1667–1674.

27 N. Moldovan, K.-H. Kim and H. D. Espinosa, *J. Microelectromech. Syst.*, 2006, **15**, 204–213.

28 N. Moldovan, K. Kim and H. Espinosa, *J. Micromech. Microeng.*, 2006, **16**, 1935.

29 P. Schön, J. Geerlings, N. Tas and E. Sarajlic, *Anal. Chem.*, 2013, **85**, 8937–8942.

30 E. Sarajlic, Method of manufacturing a plurality of through-holes in a layer of first material, *US Patent 10207244*, 2019.

31 R. B. Bird, W. E. Stewart and E. N. Lightfoot, *Transport phenomena*, John Wiley & Sons, 2007.

32 P. Galambos and F. K. Forster, *Micro Total Analysis Systems*, 1998, pp. 189–192.

33 A. Prosperetti and G. Tryggvason, *Computational methods for multiphase flow*, Cambridge University Press, 2009.

34 M. Madadelahi, E. Ghazimirsaeed and A. Shamloo, *Anal. Chim. Acta*, 2019, **1068**, 28–40.

35 K. W. Oh, K. Lee, B. Ahn and E. P. Furlani, *Lab Chip*, 2012, **12**, 515–545.

36 B. J. Kirby, *Micro-and nanoscale fluid mechanics: transport in microfluidic devices*, Cambridge University Press, 2010.

37 A. Ajdari, N. Bontoux and H. A. Stone, *Anal. Chem.*, 2006, **78**, 387–392.

38 X. Yan, M. Liu, J. Zhang, H. Zhu, Y. Li and K. Liang, *Microfluid. Nanofluid.*, 2015, **19**, 435–445.

39 H. Ahn and S. Brandani, *AIChE J.*, 2005, **51**, 1980–1990.

40 G. I. Taylor, *Proc. R. Soc. London, Ser. A*, 1953, **219**, 186–203.

41 I. L. Ahmad, M. R. Ahmad, M. Takeuchi, M. Nakajima and Y. Hasegawa, *IEEE Trans. Biomed. Circuits Syst.*, 2017, **11**, 1413–1421.

42 H. Bruus, *Theoretical microfluidics, Oxford University Press Oxford*, 2008, vol. 18.

43 R. R. Grüter, J. Vörös and T. Zambelli, *Nanoscale*, 2013, **5**, 1097–1104.

44 X. Cao, R. de Gruiter, R. van Oorschot, S. Baldi, H. HosseinNia and M. K. Ghatkesar, *Proc. Int. Fed. Autom. Control World Congr.*, 2017, **50**, 15542–15547.

45 H. Song, D. L. Chen and R. F. Ismagilov, *Angew. Chem., Int. Ed.*, 2006, **45**, 7336–7356.